

Ridgecrest aftershocks at Coso suppressed by thermal destressing

<https://doi.org/10.1038/s41586-021-03601-4>

Kyungjae Im^{1✉}, Jean-Philippe Avouac¹, Elías R. Heimisson^{1,4} & Derek Elsworth^{2,3}

Received: 28 June 2020

Accepted: 30 April 2021

Published online: 30 June 2021

 Check for updates

Geothermal and volcanic areas are prone to earthquake triggering^{1,2}. The Coso geothermal field in California lies just north of the surface ruptures driven by the 2019 Ridgecrest earthquake (moment magnitude $M_w = 7.1$), in an area where changes in coseismic stress should have triggered aftershocks^{3,4}. However, no aftershocks were observed there⁴. Here we show that 30 years of geothermal heat production at Coso depleted shear stresses within the geothermal reservoir. Thermal contraction of the reservoir initially induced substantial seismicity, as observed in the Coso geothermal reservoir, but subsequently depleted the stress available to drive the aftershocks during the Ridgecrest sequence. This destressing changed the faulting style of the reservoir and impeded aftershock triggering. Although unlikely to have been the case for the Ridgecrest earthquake, such a distressed zone could, in principle, impede the propagation of a large earthquake.

The 2019 Ridgecrest earthquakes ($M_w = 6.4$ and $M_w = 7.1$) triggered a sequence of intense aftershocks that extended well north of the Coso volcanic area³ (Fig. 1a). This seismicity coincided approximately with a northwest-trending lobe of increased Coulomb stress due to the $M_w = 7.1$ mainshock⁵ (Fig. 1b). However, no aftershocks were detected within the geothermal field area, which lies within the lobe of increased Coulomb stress⁴ (Fig. 1). This gap in aftershocks at Coso is unexpected because geothermal and volcanic areas are prone to remote triggering⁶ and because geothermal operations can trigger intense seismicity^{7,8}. Here we demonstrate that this feature is real and use numerical simulations to show that it resulted from destressing due to the geothermal operation.

The lack of aftershocks at Coso could be interpreted to reflect the locally shallower seismogenic depth range. Seismicity cuts off at a shallow depth of around 4 km within the Coso field area (Fig. 1c), probably owing to a shallow brittle–ductile transition due to the large temperature gradient⁹. Away from Coso, the seismicity extends to the typical 10–15 km depth of the seismogenic zone in California¹⁰. According to this explanation, we would expect a rate of aftershocks about three to four times lower at Coso than elsewhere. However, even if we assume that the after-Ridgecrest seismicity is entirely aftershock (that is, no contribution from the geothermal operation), the catalogue shows an aftershock rate about 20 times lower than in the areas immediately northwest or southeast of the geothermal field (Extended Data Fig. 1). We therefore conclude that the lack of aftershocks truly reflects a lower sensitivity of the geothermal field to static triggering. A recent study¹¹ based on a local seismic network reports more aftershocks at Coso than observed by the regional network. These data, once declustered, show that areas around the geothermal field experienced an increased rate of seismicity after the Ridgecrest earthquake. However, although the reservoir was included in the analysis, it could not be independently resolved owing to the declustering. Another recent study, with

non-declustered local seismic network data, shows that the Ridgecrest earthquake did not affect the total seismicity rate within the reservoir¹².

Geothermal power production at Coso started in 1987 with an electrical power capacity of 230 MW¹³. This large-scale operation induced substantial ground deformation and seismicity. Subsidence measured using interferometric synthetic aperture radar (InSAR) exceeded 14 cm over the injection area between September 1993 and June 1998¹⁴ and was most probably driven by thermal contraction and pressure depletion, as commonly observed over other geothermal fields¹⁵. There may also be natural tectonic or magmatic sources of vertical deformation in the Coso area¹⁶, but it seems unlikely that these sources could explain the deformation signal measured from InSAR, owing to the strong correlation between the signal and the geothermal field operation. Recent InSAR observations show continued subsidence, but at a lower rate (Fig. 2f).

The paucity of aftershocks during the 2019 Ridgecrest earthquake sequence is surprising because the Coso reservoir has been seismically active since the beginning of geothermal field development in 1981¹⁰ (Fig. 1a, c, grey circles). We consider the time evolution of seismicity within the Coso reservoir before 2019. Seismicity ramped up substantially when geothermal power production started in 1987, peaking after around 10 years of production (Fig. 1d). We identify spatiotemporal evolution of seismicity that reflects the details of the geothermal field development (Extended Data Fig. 2). For example, an early transient peak in 1984 probably coincides with a stimulation or testing phase. A more recent peak is due to the development of the East Flank area after 2000. The overall evolution is dominated by the seismicity within the main field, which gradually increased, peaked about 10 years after the beginning of geothermal production and decreased substantially afterwards.

Reservoir pressure has been monotonically decreasing during production¹⁷, a feature consistent with production exceeding injection (Fig. 2a). The pressure drop must have induced a gradual decrease in Coulomb stress (increase in effective normal stress), so it cannot explain

¹Geology and Planetary Science Division, California Institute of Technology, Pasadena, CA, USA. ²Energy and Mineral Engineering and Geosciences, EMS Energy Institute, Pennsylvania State University, University Park, PA, USA. ³G3 Center, Pennsylvania State University, University Park, PA, USA. ⁴Present address: Swiss Seismological Service, ETH Zurich, Zurich, Switzerland.

✉e-mail: kjim@caltech.edu

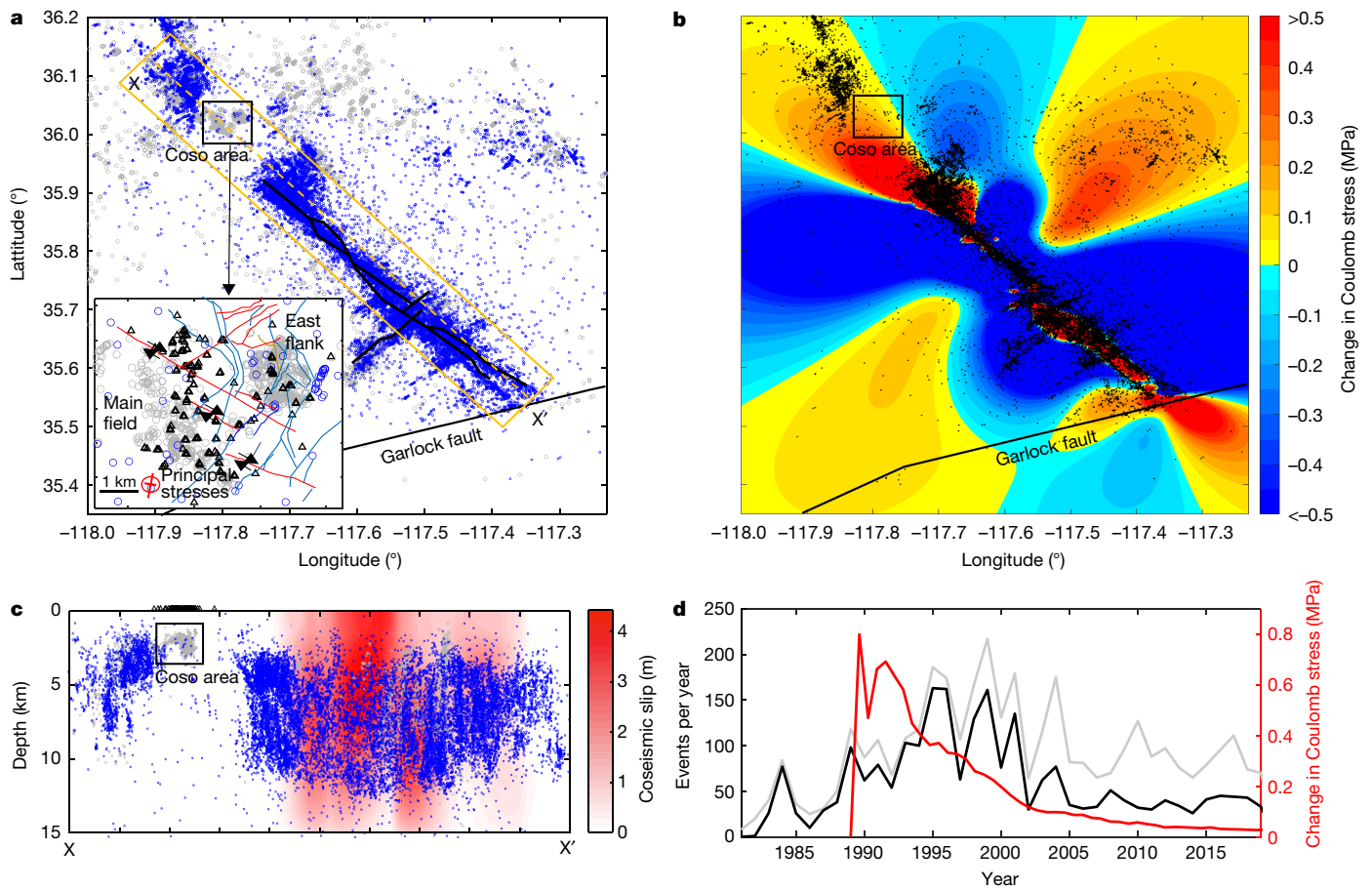


Fig. 1 | Ridgecrest aftershock and prior seismicity in the Coso area. **a**, Relocated seismicity¹⁰ ($M_w > 1$) before (since 2010; grey circles) and after (until the end of 2019; blue circles) the 2019 $M_w = 7.1$ mainshock. The black lines indicate the surface ruptures of the $M_w = 7.1$ and $M_w = 6.4$ earthquakes of 2019³. Inset, close-up view of the Coso geothermal field. Solid lines represent strike-slip faults parallel to surface ruptures of Ridgecrest earthquake (red) and normal (blue) faults^{26,27}; triangles indicate the locations of geothermal wells (<https://maps.conservation.ca.gov/doggr>). The red symbol in the inset represents the orientations and relative magnitude of the principal stresses (lines, horizontal; circle, vertical)^{26,27}. **b**, Changes in static Coulomb stress due to the $M_w = 7.1$ mainshock, calculated for a right-lateral fault parallel to the main

faults ruptured in these events (red faults in inset **a**). We used source models derived from remote sensing and high-rate GPS data⁵, assuming a coefficient of friction 0.6. Black circles indicate Ridgecrest aftershocks. **c**, Depth distribution of earthquakes in section XX' in **a** (all events in the orange box in **a**), along with the coseismic slip distribution⁵ (red colour scale). **d**, Yearly rate of $M_w > 1$ earthquakes (grey circles in **a** and **c**) in the main field (black, left axis; Extended Data Fig. 1c–e) and in the entire Coso area (main field and east flank; grey, left axis), and simulated change in Coulomb stress at the centre of the reservoir (red, right axis; Fig. 3a). See Extended Data Figs. 1–3 for detailed seismicity history.

the sustained seismicity observed in the reservoir. Hence, another effect that increases Coulomb stress, such as thermal destressing, is required. Changes in thermoporoelastic stress may be substantial, owing to elastic coupling¹⁸, and may trigger seismicity at relatively large distances from the boreholes^{18,19}. An initial flow test in the Coso area showed a gradual increase in permeability associated with a decrease in injection pressure by around 0.5 MPa over 40 days²⁰. This observation also points to a dominating thermal effect. Fracturing and faulting induced by thermal contraction tend to enhance permeability²¹. By contrast, the pressure reduction should have prevented faulting and allowed for fracture closing, resulting in a decrease in permeability.

Thermal effects evolve slowly and may considerably modify the state of stress^{21–23} and affect the depth of the brittle–ductile transition. The seismicity in the reservoir area clearly migrated to a greater depth during the field operation, as would be expected from reservoir cooling (Fig. 2c). There is also a hint in the time evolution of focal mechanisms within the Coso area²⁴ that the stress field was substantially altered during geothermal production. The decrease in seismicity after the peak in the 1990s coincides with an increase in the diversity of focal mechanisms and in the proportion of normal faulting events (Extended Data Fig. 3).

We therefore hypothesize that the cumulative stress changes induced by geothermal heat production from Coso since 1987 impeded earthquake triggering during the 2019 Ridgecrest earthquake sequence.

We model the geomechanical effect of the geothermal operation using the thermohydraulic simulator TOUGH–FLAC²⁵ (Methods). The simulations were designed using public information on the geothermal field operation (<https://openei.org/>, <https://maps.conservation.ca.gov/doggr/>) and previous studies^{26–28}. The Coso geothermal field consists of more than 100 wells, which were developed sequentially over the 30 years of production, in an area with multiple strike-slip (dominant in the main field area) and normal (dominant in the east flank area) faults (Fig. 1a, inset). The first successful production well was completed in 1981, but large-scale production did not start until 1987, once the development of the main field was completed. The development of the east flank area started in the early 2000s^{27,28}. We consider a simplified setting consistent with the size of the developed area and constrained by reported flow rates and energy production. Our model consists of 50 wells (25 injectors and 25 producers at depths of 1,800 m and 1,300 m) in a 4 km × 4 km × 3 km reservoir, which is embedded in a 30 km × 30 km × 18 km domain (Extended Data Fig. 4). The reservoir and

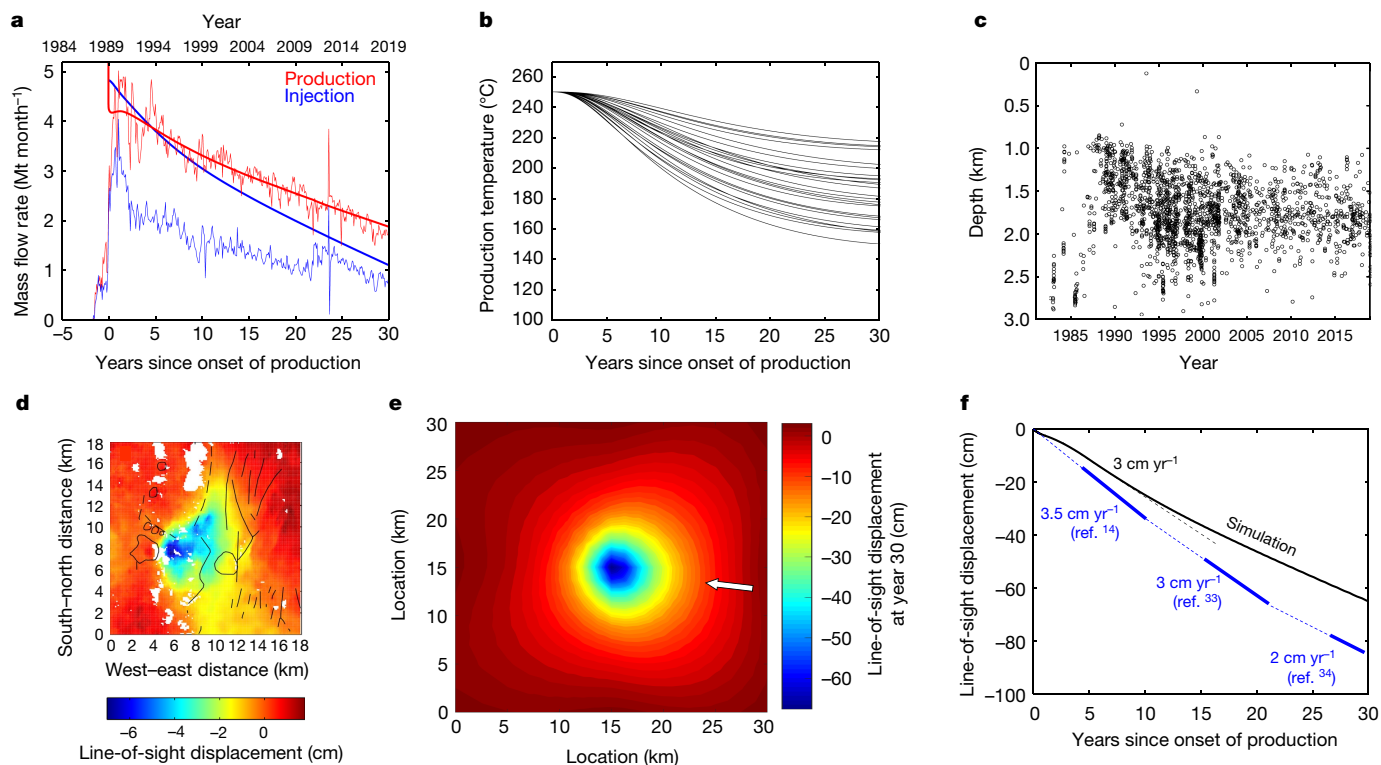


Fig. 2 | Production, power generation and surface subsidence for our reference simulation. **a**, Reported injection (blue) and production (red) flow rates from the Coso field (thin lines), with simulation results superimposed (bold lines). The onset of production is set to 1 January 1989 in the simulation. **b**, Predicted change in temperature since the onset of production at all 25 producing wells. **c**, Time evolution of earthquake ($M_w > 1$) depth in the Coso main field. The migration towards greater depths is consistent with the cooling of the reservoir. **d**, Cumulative line-of-sight displacement over the Coso area, recovered from InSAR measurements between May 1996 and June 1998. Image

adapted with permission from ref. ¹⁴, American Geophysical Union. **e**, Predicted cumulative line-of-sight displacement after 30 years of production. The arrow shows the line-of-sight unit vector (0.38, -0.09, 0.92)¹⁴ surface deformation (see Extended Data Fig. 7 for separate x , y and z components). **f**, Time evolution of the maximum line-of-sight displacement (solid black line) and observed line-of-sight displacement rates (solid blue solid)^{14,33,34}, with their extrapolations (blue dashed lines). The black dashed line indicates the maximum displacement rate at years 5–7.

cap are assigned a bulk Mohr–Coulomb rheology, with a cohesion of 2 MPa and a friction coefficient of 0.6 (or 0.3), with the medium outside the reservoir and cap considered fully elastic. All elements are assigned a volumetric thermal contraction coefficient of $6.0 \times 10^{-5} \text{ K}^{-1}$, consistent with laboratory measurements at 250 °C²⁹. Vertical stress is controlled by gravitational loading; horizontal stresses are applied on the boundary, consistent with a previous study of the local stress field^{26–28} (Methods).

Reservoir cooling is driven mainly by fluid advection associated with the cold-water injection and therefore depends primarily on the flow rate. Hence, the flow rate is a dominating factor in defining the change in reservoir temperature. The data reported by the operator show production rates of nearly double the injection rates (Fig. 2a). The excess production must have been balanced by either a reduction in the pore volume or an influx of groundwater in the reservoir. The cumulated excess volume of around $5.3 \times 10^8 \text{ m}^3$ (assuming 1 ton $\approx 1 \text{ m}^3$) would require an unrealistic pressure drop of around 400 MPa (assuming a roughly 2 km \times 2 km \times 4 km reservoir with a bulk modulus of 13 GPa). The excess production was therefore probably compensated by substantial groundwater supply. This inference is consistent with geochemical evidence of recharge from a shallow cold aquifer and from regional groundwater³⁰. It also implies that the reservoir pore space is partly filled with steam due to vaporization. Because our simulation assumes a hydraulically closed domain boundary and single-phase flow, fitting both the production and the injection data would require an unreasonably large drop in pore pressure. We therefore carried out simulations targeted to fit either the production (Fig. 2a) or the injection rates. We choose the first scenario as a reference as it is probably more realistic because

the excess production probably comes from colder surrounding areas or groundwater. We consider the second scenario to provide a lower bound on thermal effects (Extended Data Fig. 5). Even our reference scenario may underestimate thermal contraction because it ignores the cooling effect of evaporation implied by the continuous increase of the steam fraction in the produced flow over the operation period³¹.

Our simulations account for the continuous decrease in pressure by controlling the injection and production pressure (Extended Data Fig. 6). The resulting pressure drop after 30 years is approximately 5.5 MPa in the reservoir and decreases gradually beyond it (Extended Data Fig. 6b). The predicted rate of decrease in pressure (around 0.18 MPa yr⁻¹) matches the reported rate (around 0.17 MPa yr⁻¹ during 2012–2014)¹⁷. Our simulations show that, even if heat extraction is driven by only the injection flow rate, the effect of the drop in pore pressure on stress changes is only a fraction of the thermal stresses.

In our reference simulation, the production temperature decreases from 250 °C (year 0) to between 150 °C and 210 °C after 30 years (Fig. 2b). This simulation initially yields electricity generation of about 170 MW, which declines over time to about 50 MW, assuming an average efficiency of the geothermal power plant of 12%³². This estimate is smaller than the reported power output capacity (230 MW)¹³, but gets closer if we assume 16% efficiency, which is the upper bound for double-flash power plants (the technology used at Coso)³². This comparison shows that the heat extraction predicted in our simulation may be similar to, or slightly smaller than, that in reality.

Our reference simulation predicts cumulative surface line-of-sight displacement with a pattern and amplitude (about 65 cm over 30 years)

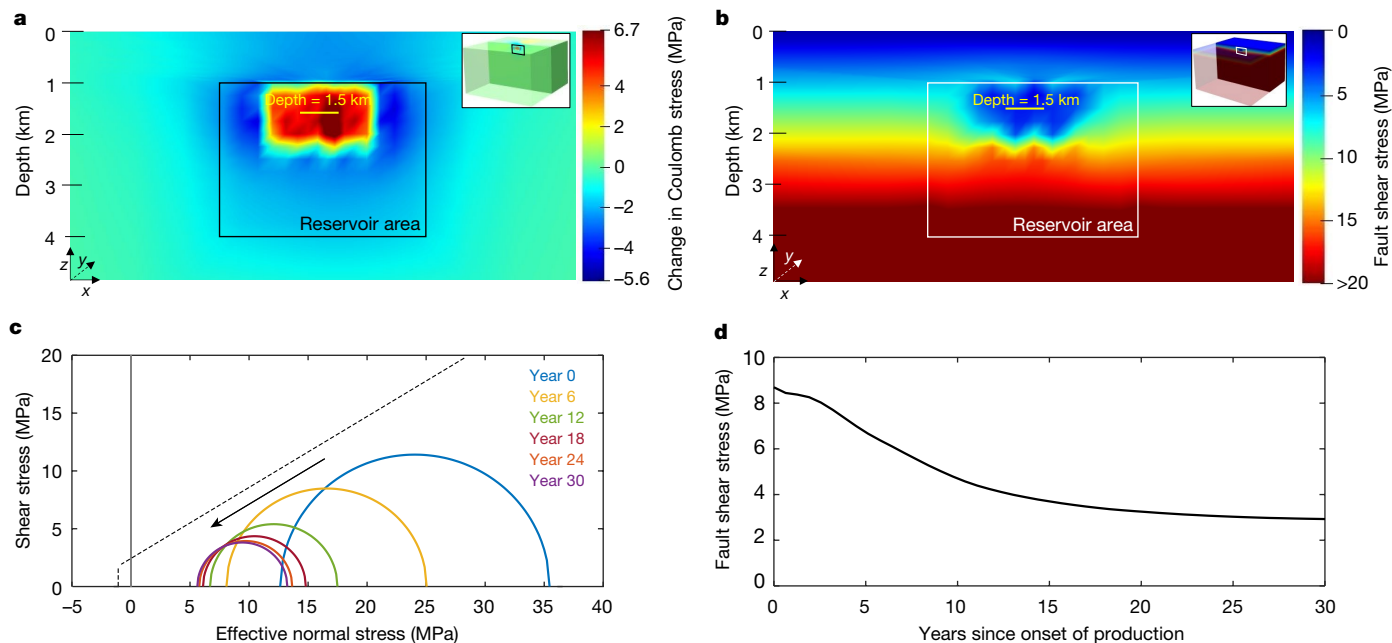


Fig. 3 | Simulation of stress changes due to thermal contraction, pore pressure changes and anelastic failure of the reservoir. a, Change in Coulomb stress at the end of the simulation (year 30), calculated on faults parallel to the $M_w = 7.1$ rupture on a cross-section through the reservoir area (see inset). **b,** Shear (xy) stress at the end of the simulation (year 30) for the same cross-section as in **a**. **c,** Mohr circle representation of the evolution of stress at the centre of the reservoir during the simulation (stresses are

averaged along the yellow line in **a** and **b**). The Mohr circles do not touch the failure envelope because failure occurs only in a fraction of the reservoir volume, close to the injection wellbore. The grey dashed line indicates the input failure criteria in this simulation: tensile cut-off, 1 MPa; cohesion, 2 MPa; friction, 0.6. **d,** Change in shear (xy) stress at the centre of the reservoir (averaged along the yellow line in **a** and **b**).

that are generally consistent with the InSAR data^{14,33,34} (Fig. 2d–f). The peak deformation rate is about 3.0 cm yr^{-1} in our simulation (Fig. 2f), comparable to the observed value¹⁴ of about 3.5 cm yr^{-1} . In general, our reference model provides a reasonable estimate of the strain change within the reservoir. We conducted additional simulations without thermal stress (Extended Data Fig. 8) and found that the pressure depletion could, in principle, contribute about 57% of total subsidence. Because the pressure drop takes place over a wider area than does thermal cooling, the surface subsidence predicted by the isothermal simulation is less localized and a poorer fit to the satellite observations (Extended Data Fig. 8). This conclusion conflicts with the claim³⁵ that the subsidence in the Coso area is mostly driven by pressure. If the pressure effect was dominant, it would not explain the sustained seismicity during the geothermal field operation at Coso. Thermal effects help to reconcile surface deformation with seismicity.

Thermal contraction results in a decrease in the compressive normal stresses, shifting the Mohr circles progressively towards the Mohr–Coulomb failure envelope (Fig. 3c). As a result, some reservoir areas fail, resulting in a gradual decrease in the differential stress. Failure limits the decrease in the minimum principal stress so that the Mohr circle shrinks in diameter, leading to a very large decrease in shear stress in the reservoir (Fig. 3). We also conducted simulations assuming a purely elastic reservoir. In this case, there is no reduction in shear stress and tensile stress at the centre of the reservoir becomes unrealistically large (18 MPa; Extended Data Fig. 10). Such large tensile stresses are not possible in reality, because of the limited strength of the rocks that comprise the reservoir.

Our model predicts that the shear stress decreases from an initial value of about 9 MPa to about 2.9 MPa after 30 years of operation (Fig. 3d). Because friction tends to be reduced at higher temperatures, we also tested a case with lower internal friction (0.3 instead of 0.6 for the reference model). We found that the final shear stress is even smaller with lower friction (Extended Data Fig. 9). The decrease in shear stress explains the gap in large aftershocks ($M_w > 1$) detected by the regional

seismic network in the Coso area in 2019. According to our simulation, the differential stress (the difference between the maximum and minimum principal stresses, which are both horizontal) decreases from about 30 MPa to less than 10 MPa (Extended Data Fig. 3d–f). At the injector depth, the maximum horizontal stress decreases gradually to the vertical stress and eventually even lower. Such evolution should, in principle, favour normal faulting events. Above the reservoir, at a depth shallower than about 1 km, the vertical stress becomes smaller than the minimum horizontal stress, so thrust events should eventually be favoured. This evolution of the stress field is qualitatively consistent with the increasing diversity of focal mechanisms observed during the geothermal field operation (Extended Data Fig. 3).

The predicted stress evolution is also consistent with the evolution of seismicity. According to our model, the Coulomb stress on faults parallel to the Ridgecrest rupture initially increased by as much as 6.7 MPa, owing to thermal contraction of the reservoir (Fig. 3a). This stress increased rapidly, by around $0.6\text{--}0.8 \text{ MPa yr}^{-1}$, during the first 3 years before slowly decreasing to less than 0.1 MPa yr^{-1} at the end of the simulation (Fig. 1d). Thus, the observed seismicity rate approximately follows the simulated Coulomb stress rate, as would be expected from a standard Coulomb failure model with an instantaneous drop in coseismic stress³⁶. In reality, the response of the seismicity should be damped because earthquake nucleation is a time-dependent process³⁷. The effect of nucleation can probably be neglected on a multiyear timescale³⁶.

Although poor sensitivity to dynamic triggering in the Coso geothermal field has been reported³⁸, this observation is questioned by recent studies^{11,39}. The suggested mechanism³⁸, which involves unclogging of fluid pathways and subsequent pore pressure equalization, is unlikely to explain the paucity of aftershocks at Coso in 2019. A homogenous pore pressure should not inhibit static triggering of earthquakes by the increase in coseismic Coulomb stress.

Although thermal contraction of the reservoir induced considerable seismicity^{1,40}, it eventually depleted the stress available to drive

the aftershocks during the Ridgecrest sequence. This destressing results from anelastic but mostly aseismic deformation. The total released seismic moment calculated by summing the scalar moments of the events¹⁰ in the main field area is 2.1×10^{15} N m. Using the Kostrov approach⁴¹, this seismicity accounts for a shear strain of at most 1.3×10^{-5} , a value estimated by considering a $2 \text{ km} \times 2 \text{ km} \times 2 \text{ km}$ volume of rock with a shear modulus of 10 GPa and assuming that all events occurred on parallel fault planes. This strain is about two orders of magnitude smaller than the maximum anelastic shear strain predicted by our simulation (about 1.1×10^{-3} ; Extended Data Fig. 11), which implies that the deformation of the Coso reservoir was mostly aseismic. This result is in agreement with the theoretical considerations and with observational evidence from fluid injection experiments and geothermal operations^{42–45}, which all suggest that faults tend to creep aseismically at low normal effective stresses.

We conclude that seismic and aseismic anelastic deformation induced by the geothermal operations at Coso probably substantially released the shear stress initially available to drive earthquakes. The thermal destressing of the Coso area reduced aftershock productivity. Such destressing could, in principle, form a barrier to the propagation of a large earthquake. However, the shallow brittle–ductile transition beneath the broader Coso volcanic area is a more likely cause of the arrest of the rupture in 2019, given that the rupture stopped about 10 km away from the geothermal field. The observed reduction in aftershock productivity may provide a general model of the early-time potential for induced earthquake mitigation, if project-terminating, triggered seismicity in deep geothermal projects^{46–48} can be avoided and long-term seismicity⁴⁹ is reduced to acceptable levels.

Online content

Any methods, additional references, Nature Research reporting summaries, source data, extended data, supplementary information, acknowledgements, peer review information; details of author contributions and competing interests; and statements of data and code availability are available at <https://doi.org/10.1038/s41586-021-03601-4>.

- Zang, A. et al. Analysis of induced seismicity in geothermal reservoirs – an overview. *Geothermics* **52**, 6–21 (2014).
- Kim, K.-H. et al. Assessing whether the 2017 M_w 5.4 Pohang earthquake in South Korea was an induced event. *Science* **360**, 1007–1009 (2018).
- Ross, Z. E. et al. Hierarchical interlocked orthogonal faulting in the 2019 Ridgecrest earthquake sequence. *Science* **366**, 346–351 (2019).
- Hardebeck, J. L. A stress-similarity triggering model for aftershocks of the M_w 6.4 and 7.1 Ridgecrest earthquakes. *Bull. Seismol. Soc. Am.* **110**, 1716–1727 (2020).
- Chen, K. et al. Cascading and pulse-like ruptures during the 2019 Ridgecrest earthquakes in the Eastern California Shear Zone. *Nat. Commun.* **11**, 22 (2020).
- Hill, D. P. et al. Seismicity remotely triggered by the magnitude 7.3 Landers, California, earthquake. *Science* **260**, 1617–1623 (1993).
- Grigoli, F. et al. The November 2017 M_w 5.5 Pohang earthquake: a possible case of induced seismicity in South Korea. *Science* **360**, 1003–1006 (2018).
- Deichmann, N. & Giardini, D. Earthquakes induced by the stimulation of an enhanced geothermal system below Basel (Switzerland). *Seismol. Res. Lett.* **80**, 784–798 (2009).
- Hauksson, E. & Unruh, J. Regional tectonics of the Coso geothermal area along the intracontinental plate boundary in central eastern California: three-dimensional V_p and V_p/V_s models, spatial-temporal seismicity patterns, and seismogenic deformation. *J. Geophys. Res. Solid Earth* **112**, B06309 (2007).
- Hauksson, E., Yang, W. & Shearer, P. M. Waveform relocated earthquake catalog for Southern California (1981 to June 2011). *Bull. Seismol. Soc. Am.* **102**, 2239–2244 (2012).
- Kaven, J. O. Seismicity rate change at the Coso geothermal field following the July 2019 Ridgecrest earthquakes. *Bull. Seismol. Soc. Am.* **110**, 1728–1735 (2020).
- Blake, K. et al. Updated shallow temperature survey and resource evolution for the Coso geothermal field. In *Proc. World Geotherm. Congr.* (2020).
- Bertani, R. World geothermal power generation in the period 2001–2005. *Geothermics* **34**, 651–690 (2005).
- Fialko, Y. & Simons, M. Deformation and seismicity in the Coso geothermal area, Inyo County, California: observations and modeling using satellite radar interferometry. *J. Geophys. Res. Solid Earth* **105**, 21781–21793 (2000).
- Reinisch, E. C., Cardiff, M., Kreemer, C., Akerley, J. & Feigl, K. L. Time-series analysis of volume change at Brady Hot Springs, Nevada, USA, using geodetic data from 2003–2018. *J. Geophys. Res. Solid Earth* **125**, B017816 (2020).
- Wicks, C. W., Thatcher, W., Monastero, F. C. & Hasting, M. A. Steady state deformation of the Coso Range, east central California, inferred from satellite radar interferometry. *J. Geophys. Res. Solid Earth* **106**, 13769–13780 (2001).
- Blankenship, D. A. et al. *Frontier Observatory for Research in Geothermal Energy: Phase 1 Topical Report West Flank of Coso*, CA. Report No. 1455367, <https://doi.org/10.2172/1455367> (US Department of Energy, 2016).
- Goebel, T. H. W. & Brodsky, E. E. The spatial footprint of injection wells in a global compilation of induced earthquake sequences. *Science* **361**, 899–904 (2018).
- Goebel, T. H. W., Weingarten, M., Chen, X., Haffener, J. & Brodsky, E. E. The 2016 M_w 5.1 Fairview, Oklahoma earthquakes: evidence for long-range poroelastic triggering at >40 km from fluid disposal wells. *Earth Planet. Sci. Lett.* **472**, 50–61 (2017).
- Sanyal, S., Menzies, A., Granados, E., Sugine, S. & Gentner, R. Long term testing of geothermal wells in the Coso hot springs KGRA. In *Proc. 12th Work. Geotherm. Reserv. Eng.* 37–44 (1987).
- Im, K., Elsworth, D., Guglielmi, Y. & Mattioli, G. S. Geodetic imaging of thermal deformation in geothermal reservoirs – production, depletion and fault reactivation. *J. Volcanol. Geotherm. Res.* **338**, 79–91 (2017).
- Rutqvist, J., Wu, Y.-S., Tsang, C.-F. & Bodvarsson, G. A modeling approach for analysis of coupled multiphase fluid flow, heat transfer, and deformation in fractured porous rock. *Int. J. Rock Mech. Min. Sci.* **39**, 429–442 (2002).
- Segall, P. & Fitzgerald, S. D. A note on induced stress changes in hydrocarbon and geothermal reservoirs. *Tectonophysics* **289**, 117–128 (1998).
- Yang, W., Hauksson, E. & Shearer, P. M. Computing a large refined catalog of focal mechanisms for southern California (1981–2010): temporal stability of the style of faulting. *Bull. Seismol. Soc. Am.* **102**, 1179–1194 (2012).
- Taron, J., Elsworth, D. & Min, K.-B. Numerical simulation of thermal-hydrologic-mechanical processes in deformable, fractured porous media. *Int. J. Rock Mech. Min. Sci.* **46**, 842–854 (2009).
- Feng, Q. & Lees, J. M. Microseismicity, stress, and fracture in the Coso geothermal field, California. *Tectonophysics* **289**, 221–238 (1998).
- Davatzes, N. C. & Hickman, S. H. Stress and Faulting in the Coso Geothermal Field: Update and Recent Results from the East Flank and Coso Wash. In *Proc. 31st Work. Geotherm. Reserv. Eng.* (2006).
- Rose, P. et al. An enhanced geothermal system at Coso, California – recent accomplishments. In *Proc. World Geotherm. Congr.* (2005).
- Cooper, H. W. & Simmons, G. The effect of cracks on the thermal expansion of rocks. *Earth Planet. Sci. Lett.* **36**, 404–412 (1977).
- Spang, F. Jr. *Hydrogeologic Investigation of Coso Hot Springs, Inyo County, California*. Report No. 6025, <https://www.ekrcrd.org/files/bcdf564af/Hydrogeologic+Investigation+of+Coso+Hot+Springs.pdf> (Naval Weapons Center, 1978).
- MHA Environmental Consulting. *Coso Operating Company Hay Ranch Water Extraction and Delivery System. Conditional Use Permit (CUP 2007-003) Application*. Report No. SCH 2007101002, https://www.inyowater.org/wp-content/uploads/legacy/INDEX_DOCS/Coso%20Hay%20Ranch_FEIR_Dec_30_08.pdf (2008).
- Zarrouk, S. J. & Moon, H. Efficiency of geothermal power plants: a worldwide review. *Geothermics* **51**, 142–153 (2014).
- Ali, S. T. et al. Geodetic measurements and numerical models of deformation: examples from geothermal fields in the western United States. In *Proc. 41st Work. Geotherm. Reserv. Eng.* (2016).
- Wang, K. & Bürgmann, R. Co- and early postseismic deformation due to the 2019 Ridgecrest earthquake sequence constrained by Sentinel-1 and COSMO-SkyMed SAR data. *Seismol. Res. Lett.* **91**, 1998–2009 (2020).
- Reinisch, E. C., Ali, S. T., Cardiff, M., Kaven, J. O. & Feigl, K. L. Geodetic measurements and numerical models of deformation at Coso geothermal field, California, 2004–2016. *Remote Sens.* **12**, 225 (2020).
- Ader, T. J., Lapusta, N., Avouac, J.-P. & Ampuero, J.-P. Response of rate-and-state seismogenic faults to harmonic shear-stress perturbations. *Geophys. J. Int.* **198**, 385–413 (2014).
- Dieterich, J. A constitutive law for rate of earthquake production and its application to earthquake clustering. *J. Geophys. Res. Solid Earth* **99**, 2601–2618 (1994).
- Zhang, Q. et al. Absence of remote earthquake triggering within the Coso and Salton Sea geothermal production fields. *Geophys. Res. Lett.* **44**, 726–733 (2017).
- Alfaro-Diaz, R., Velasco, A. A., Pankow, K. L. & Kilb, D. Optimally oriented remote triggering in the Coso geothermal region. *J. Geophys. Res. Solid Earth* **125**, B019131 (2020).
- Hauksson, E. & Jones, L. M. Seismicity, stress state, and style of faulting of the Ridgecrest-Coso region from the 1930s to 2019: seismotectonics of an evolving plate boundary segment. *Bull. Seismol. Soc. Am.* **110**, 1457–1473 (2020).
- Kostrov, V. Seismic moment and energy of earthquakes, and seismic flow of rock. *Izv. Acad. Sci. USSR Phys. Solid Earth* **1**, 23–44 (1974).
- Cornet, F. H., Helm, J., Poitrenaud, H. & Etchecopar, A. Seismic and aseismic slips induced by large-scale fluid injections. *Pure Appl. Geophys.* **150**, 563–583 (1997).
- Guglielmi, Y., Cappa, F., Avouac, J.-P., Henry, P. & Elsworth, D. Seismicity triggered by fluid injection-induced aseismic slip. *Science* **348**, 1224–1226 (2015).
- Wei, S. et al. The 2012 Brawley swarm triggered by injection-induced aseismic slip. *Earth Planet. Sci. Lett.* **422**, 115–125 (2015).
- Cappa, F., Scuderi, M. M., Collettini, C., Guglielmi, Y. & Avouac, J.-P. Stabilization of fault slip by fluid injection in the laboratory and in situ. *Sci. Adv.* **5**, eaau4065 (2019).
- Kwiatk, G. et al. Controlling fluid-induced seismicity during a 6.1-km-deep geothermal stimulation in Finland. *Sci. Adv.* **5**, eaav7224 (2019).
- Hillers, G. et al. Noise-based monitoring and imaging of aseismic transient deformation induced by the 2006 Basel reservoir stimulation. *Geophysicists* **80**, KS51–KS68 (2015).
- Håring, M. O., Schanz, U., Ladner, F. & Dyer, B. C. Characterisation of the Basel 1 enhanced geothermal system. *Geothermics* **37**, 469–495 (2008).
- Gan, Q. & Elsworth, D. Thermal drawdown and late-stage seismic-slip fault reactivation in enhanced geothermal reservoirs. *J. Geophys. Res. Solid Earth* **119**, 8936–8949 (2014).

Publisher's note Springer Nature remains neutral with regard to jurisdictional claims in published maps and institutional affiliations.

© The Author(s), under exclusive licence to Springer Nature Limited 2021

Methods

We used TOUGH–FLAC²⁵ to simulate thermohydraulic processes during the geothermal operation. Stress changes within the reservoir depend on the mechanical response of the surrounding medium^{21,50}. We therefore consider a simulation domain (30 km × 30 km × 18 km) that is substantially larger than the geothermal reservoir (4 km × 4 km × 3 km). The reservoir is similar in size to the currently developed area of the Coso geothermal field.

Extended Data Fig. 4 shows the geometry and initial stress field. The domain is meshed into 13,312 blocks, which are divided into either reservoir or host blocks. All blocks are assigned a volumetric thermal contraction coefficient of $6.0 \times 10^{-5} \text{ K}^{-1}$, a bulk modulus of 13 GPa and a Poisson's ratio of 0.2. The magnitude of thermal expansion is consistent with an experimental result with quartz-rich rock at a temperature of 250 °C²⁹. Reservoir blocks (blue) are embedded at depths between 1 km and 4 km. Reservoir (blue) and upper host (dark green) are assumed to fail according to the Mohr–Coulomb criteria, with a friction coefficient of 0.6 and cohesion of 2 MPa. Lower host rock blocks (light green) are fully elastic. To achieve a stable flow rate and electricity generation, we assumed constant permeability over the entire domain. Reservoir elements have high permeabilities (16 md and 10 md for higher and lower flow rates, respectively; Extended Data Fig. 5). The host (lower and upper) block has a much smaller permeability of 0.05 md. The permeabilities were tuned to yield a production rate comparable to that of the Coso field (<https://openi.org>). See Extended Data Table 1 for model parameters.

The stress field accounts for gravity and tectonic loading. Gravitational body forces are calculated assuming an effective density (rock density minus water density) of $1,400 \text{ kg m}^{-3}$. The stress field is assumed to be initially homogeneous, with maximum and minimum horizontal stresses of 150% and 50% of the vertical stress, respectively, on the basis of a previous study of the local stress field^{26,27}. The maximum principal stress initially strikes N 20° E, which is oriented at 65° from the right-lateral strike–slip faults (Extended Data Fig. 4, inset). Rollers with shear stress are applied at the domain boundary, except at the ground surface, which is assumed to be traction-free. We tested roller and constant-stress boundary conditions at the domain boundary and found no substantial differences, confirming that the model domain is large enough. To reduce the computational cost, we assumed an initial uniform temperature of 250 °C over the domain. Also, because water density and viscosity do not depend strongly on pressure, the pressure here represents the overpressure from the hydraulic pressure (gravitational flow is ignored). Accordingly, the stresses in our simulation represent effective stresses (stress minus fluid pressure).

The Coso geothermal field consists of more than 100 wells, developed sequentially over the 30 years of production, in an area with multiple strike–slip faults. We simplified the field into 50 wellbores. The wells include 25 injectors and 25 producers, which form a five-spot pattern that accesses two depths layers (1,300 m and 1,800 m; Extended Data Fig. 4). The distance between the injectors and producers is about 500 m, slightly more closely spaced at the centre of the reservoir (Extended Data Fig. 4). We used a Peaceman well-block pressure model⁵¹, with a virtual wellbore radius of 10 cm and a Skin factor of –4 located in the well block (Extended Data Fig. 4). The initial wellbore pressure is set to 5 MPa overpressure and –1 MPa underpressure at the injector and producer wells, respectively (Extended Data Fig. 6a), and decreases with time at a different rate to achieve the target flow rate (Fig. 2a) and pressure drop (Extended Data Fig. 6).

We acknowledge that our simulation is a simplification of reality. A more realistic simulation should consider the distribution of initial pressure and temperature. In reality, the geothermal gradient is much smaller, even in the vicinity of the Coso area¹⁷. This temperature distribution affects the evolution of the reservoir temperature though fluid influx from the surrounding area. The influx from the deeper, hot zone increases the reservoir temperature, whereas the influx from all

other surroundings cools the reservoir. The cooling effect is probably much larger than the heating effect, because the cooler zone has larger contact with the reservoir, and cold water is continuously supplied from precipitation and aquifer flow. Although smaller than reality, our simulation includes considerable fluid influx (overproduction) from the surrounding area (Fig. 2a). The temperature of the influx in our simulation is probably higher than reality because we assume a uniform, high temperature (250 °C) even for the surrounding cooler area. Accordingly, if we were to use a more realistic initial temperature distribution, larger thermal destressing is expected, owing to the cold-water influx from the surroundings. Furthermore, the application of a realistic pressure gradient would induce the endothermic effect of evaporation in and above the reservoir and therefore also increase the cooling effect. Overall, we expect the application of realistic pressure and temperature gradients to enhance the thermal destressing effect relative to our simulation.

The nearly uniform thermal depletion in our simulation is not expected in a real, highly fractured reservoir. Also, a substantial change in the permeability would be expected^{21,52} with production. In reality, thermal depletion is dominant in the vicinity of existing fractures, owing to the high permeability and thermal stimulation²¹. Therefore, the thermal depletion of the fractures may become wider than predicted in our idealized depletion model. Given that the subsidence predicted by our model is comparable in extent and rate with the available observations of surface deformation, we believe that, even with these simplifications, our model provides a reasonable first-order estimate of the stress changes imparted by geothermal operations at Coso.

Data availability

The seismic catalogue¹⁰ is publicly available from the Southern California Earthquake Data Center (<https://scedc.caltech.edu/data/alt-2011-dd-hauksson-yang-shearer.html>). The Coso field well location and flow rate data are available from the California Department of Conservation (<https://maps.conservation.ca.gov/doggr/wellfinder>, <https://www.conservation.ca.gov/calgem/geothermal/manual/Pages/production.aspx>). Simulation data are available in the Caltech data repository (<https://doi.org/10.22002/D1.1455>). Source data are provided with this paper.

Code availability

The TOUGH–FLAC coupled simulator and all input files are available in the Caltech data repository (<https://doi.org/10.22002/D1.1455>).

50. Eshelby, J. D. The determination of the elastic field of an ellipsoidal inclusion, and related problems. *Proc. R. Soc. Lond. Ser. A*, **241**, 376–396 (1957)
51. Peaceman, D. W. Interpretation of well-block pressures in numerical reservoir simulation with nonsquare grid blocks and anisotropic permeability. *Soc. Pet. Eng. J.* **23**, 531–543 (1983).
52. Cappa, F. & Rutqvist, J. Modeling of coupled deformation and permeability evolution during fault reactivation induced by deep underground injection of CO₂. *Int. J. Greenh. Gas Control* **5**, 336–346 (2011).
53. Frohlich, C. Triangle diagrams: ternary graphs to display similarity and diversity of earthquake focal mechanisms. *Phys. Earth Planet. Inter.* **75**, 193–198 (1992).

Acknowledgements This study was supported by the National Science Foundation via the IUCR center Geomechanics and Mitigation of Geohazards (award number 1822214) and via the Southern California Earthquake Center (SCEC). The SCEC is funded by NSF Cooperative Agreement EAR-1600087 and USGS Cooperative Agreement G17AC00047.

Author contributions K.I. carried out the data analysis and numerical simulations. E.R.H. computed the coseismic Coulomb stress changes. D.E. provided the simulator TOUGH–FLAC. K.I. and J.-P.A. designed the study and wrote the Article. All authors edited the manuscript.

Competing interests The authors declare no competing interests.

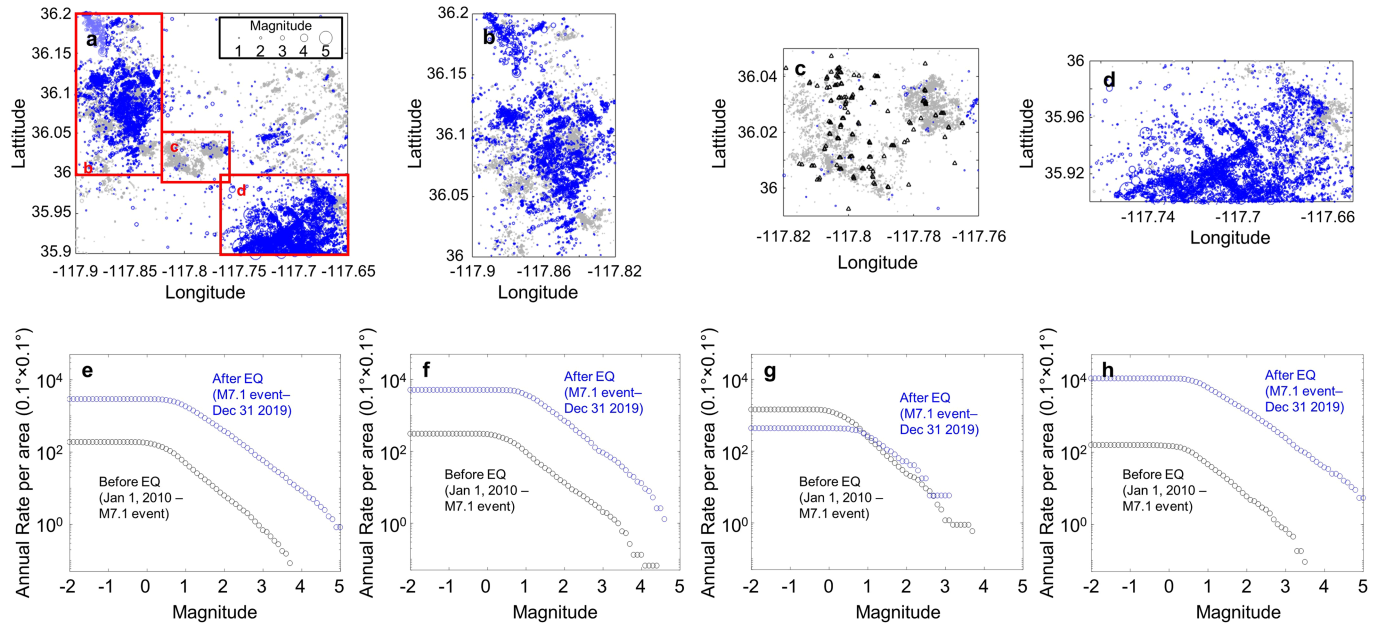
Additional information

Supplementary information The online version contains supplementary material available at <https://doi.org/10.1038/s41586-021-03601-4>.

Correspondence and requests for materials should be addressed to K.I.

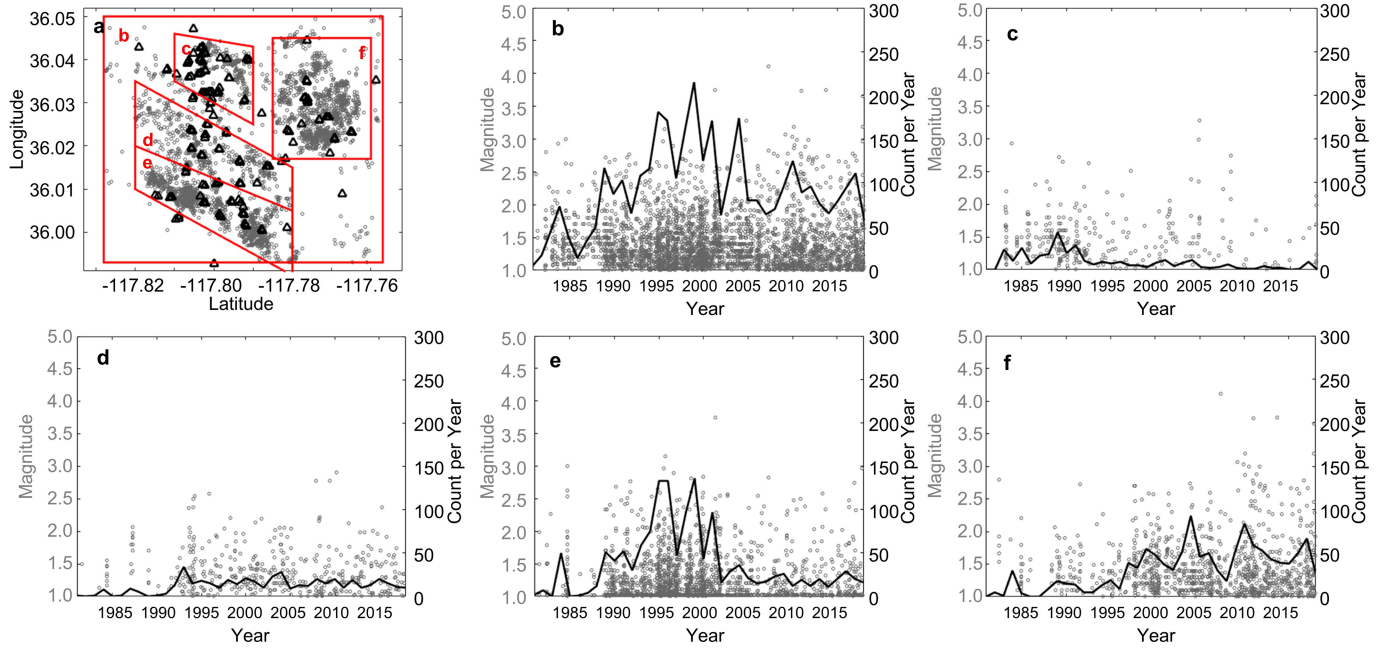
Peer review information Nature thanks Roland Burgmann, J. Ole Kaven and the other, anonymous, reviewer(s) for their contribution to the peer review of this work.

Reprints and permissions information is available at <http://www.nature.com/reprints>.



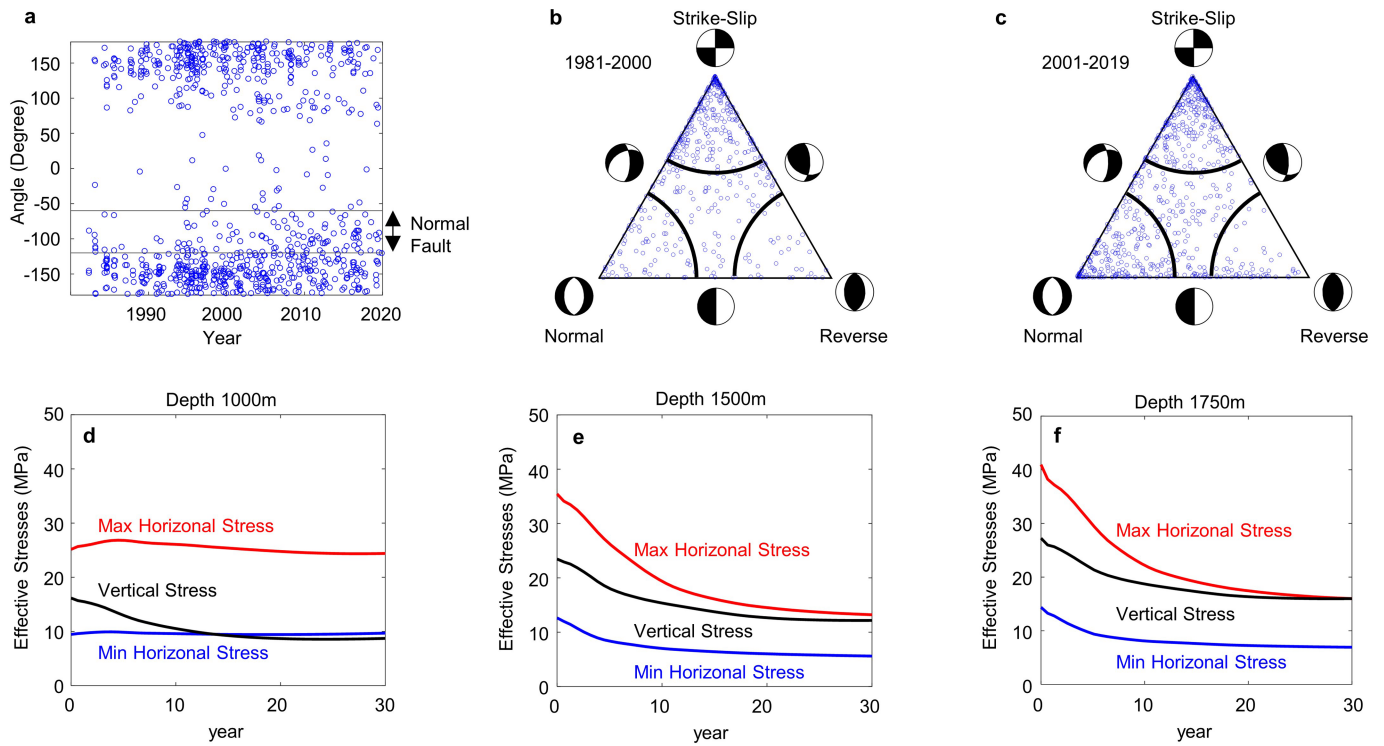
Extended Data Fig. 1 | Seismicity before and after the Ridgecrest mainshock (5 July 2019) in and around the Coso area. We divided the area into different domains. **a–d**, Relocated seismicity¹⁰ of all magnitude, before (2010 to the $M_w = 7.1$ mainshock; grey circles) and after ($M_w = 7.1$ mainshock to the end of 2019; blue circles) the Ridgecrest earthquake. **a–h**, We compare the spatial distribution (**a–d**) and cumulative magnitude–frequency distribution (**e–h**) of earthquakes before (black) and after (blue) the mainshock for the Coso

volcanic area (**a, e**), Cactus flat (**b, f**), Coso geothermal field (**c, g**) and the northwest edge of the $M_w = 7.1$ event (**d, h**). Red rectangles in **a** define the areas for each plot. Black triangles in **c** indicate the locations of geothermal wells. The density of aftershocks above the detection threshold ($M_w > 1$) is about two orders of magnitude lower in the Coso geothermal field (**c**) than in the surrounding areas (**b, d**). A similar result has been reported previously⁴.



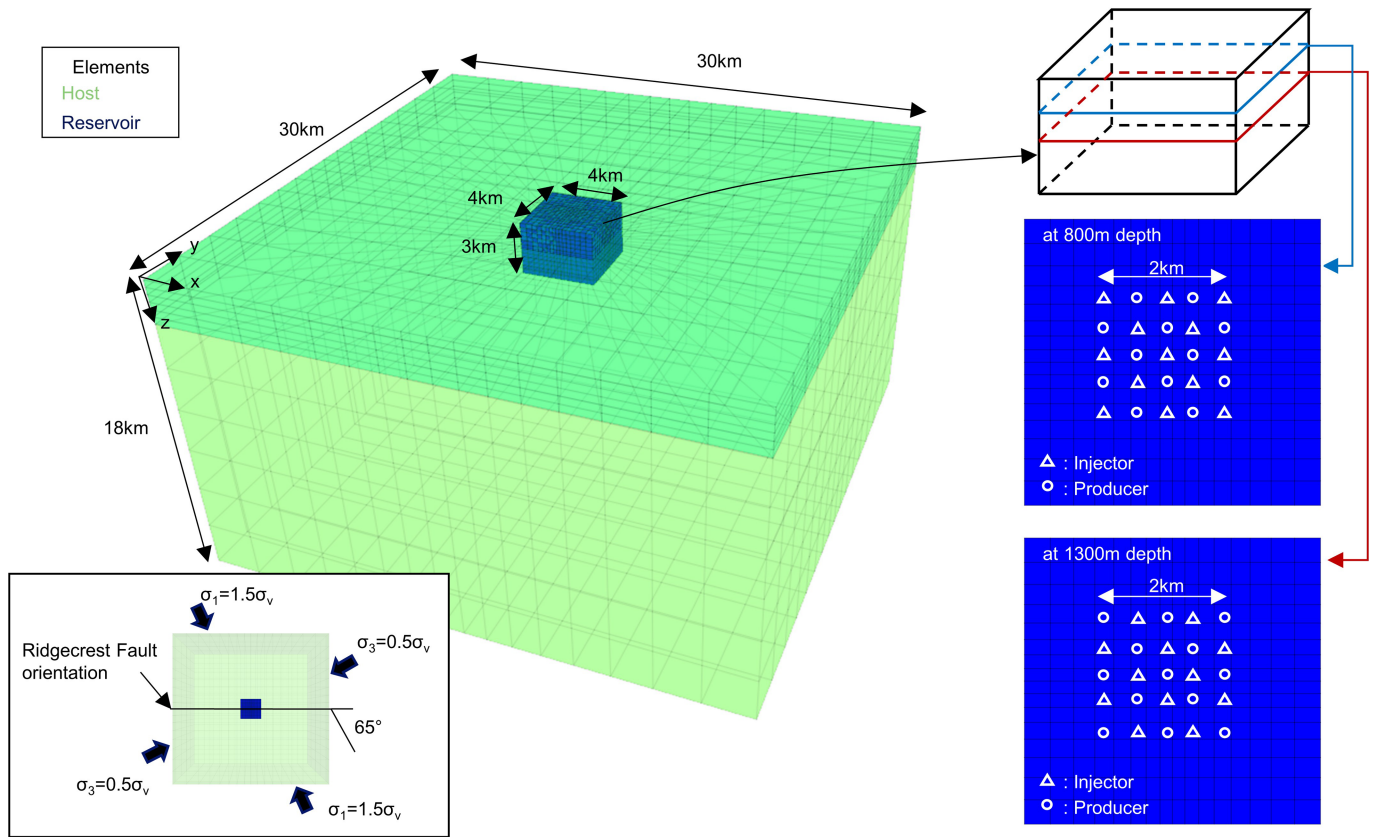
Extended Data Fig. 2 | History of seismicity in the Coso area. a, Distribution of seismicity ($M_w > 1$)¹⁰. **b,** Seismicity history over the entire Coso area. **c–f,** Seismicity history of event magnitude (circles; left axis) and annual rate (black

line; right axis) for each fault zone (**c–e,** Coso main field; **f,** east flank area), as indicated in **a**. The fault zones are selected on the basis of the expression of the seismic cloud.



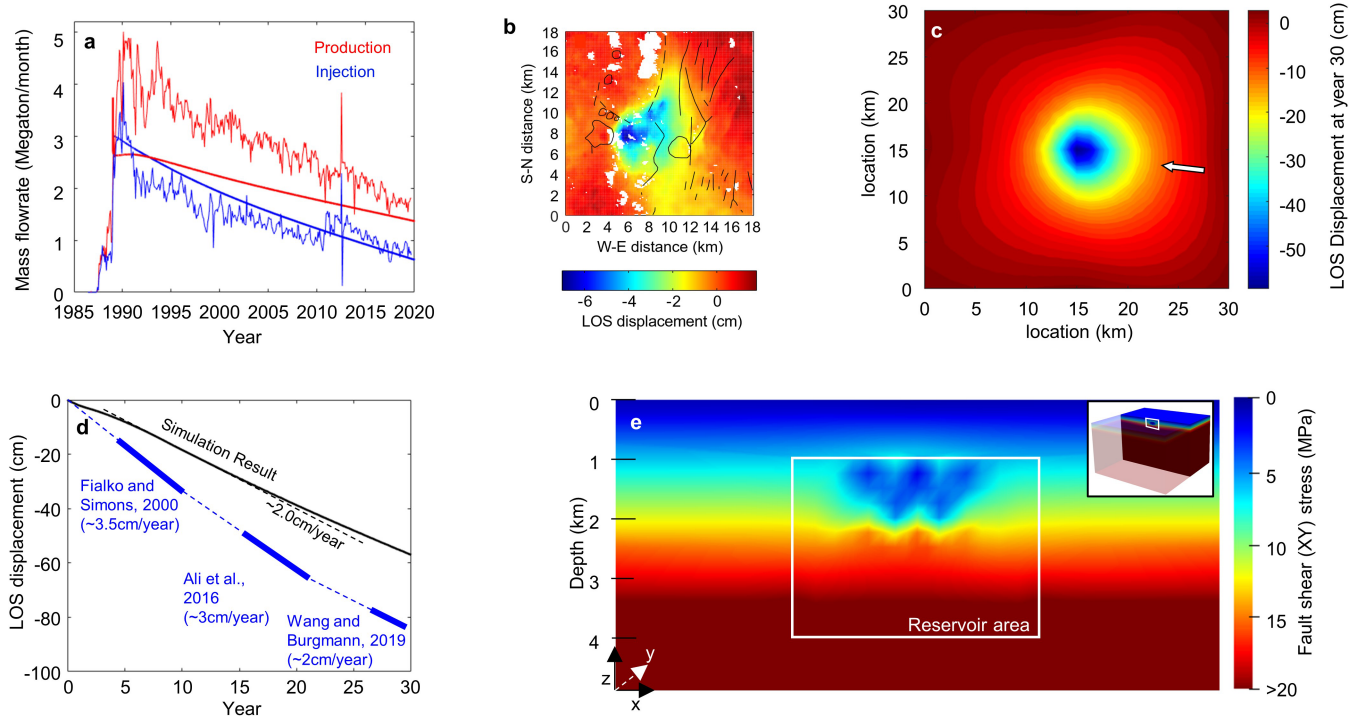
Extended Data Fig. 3 | Change of focal mechanism in the Coso main field area and effective stress changes predicted by the simulation. a, The rake angle shows that the proportion of normal faulting (-120° to about -60°) increases with time. **b, c,** Ternary plots⁵³ show that the focal mechanism is more diverse, with increased normal faulting in the later operation period (2001–2019; **c**) than in the earlier period (1981–2000; **b**). **d–f,** Time-dependent maximum horizontal (red), minimum horizontal (blue) and vertical (black)

stress at different depths, calculated as an average along a 1-km baseline at the centre of the reservoir at each depth (**d**, 1,000 m; **e**, 1,500 m; **f**, 1,750 m). The stresses within the reservoir (**e, f**) decline with time, but the rate of decline in vertical stress is lower than that in maximum horizontal stress. The simulation predicts an increase in the proportion of normal faulting and diversity of focal mechanism, as observed in **a–c**.



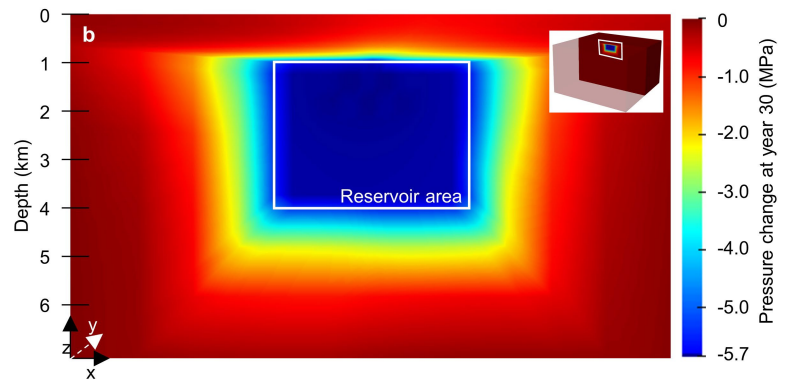
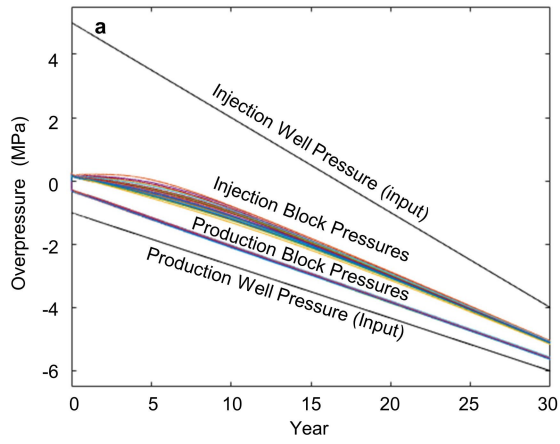
Extended Data Fig. 4 | Model description. Blue, dark green and light green blocks represent the reservoir, upper host and lower host elements, respectively. The right-hand side shows the repeating five-spot pattern of injectors (triangles) and producers (circles). Inset, initial horizontal stresses (σ_1 , maximum; σ_3 , minimum) calculated from Coso field data (Fig. 1a, inset). Vertical stress (σ_v) is calculated as gravitational stress for an effective density of

$1,400 \text{ kg m}^{-3}$ at every time step. The x axis is chosen to be parallel to the dominant fault orientation in the main field (Fig. 1a, inset), which is parallel to the main fault ruptured in the $M_w = 7.1$ Ridgecrest earthquake. Roller and shear stress boundaries are applied corresponding to the initial stress, as shown in the inset. The ground surface is stress-free.



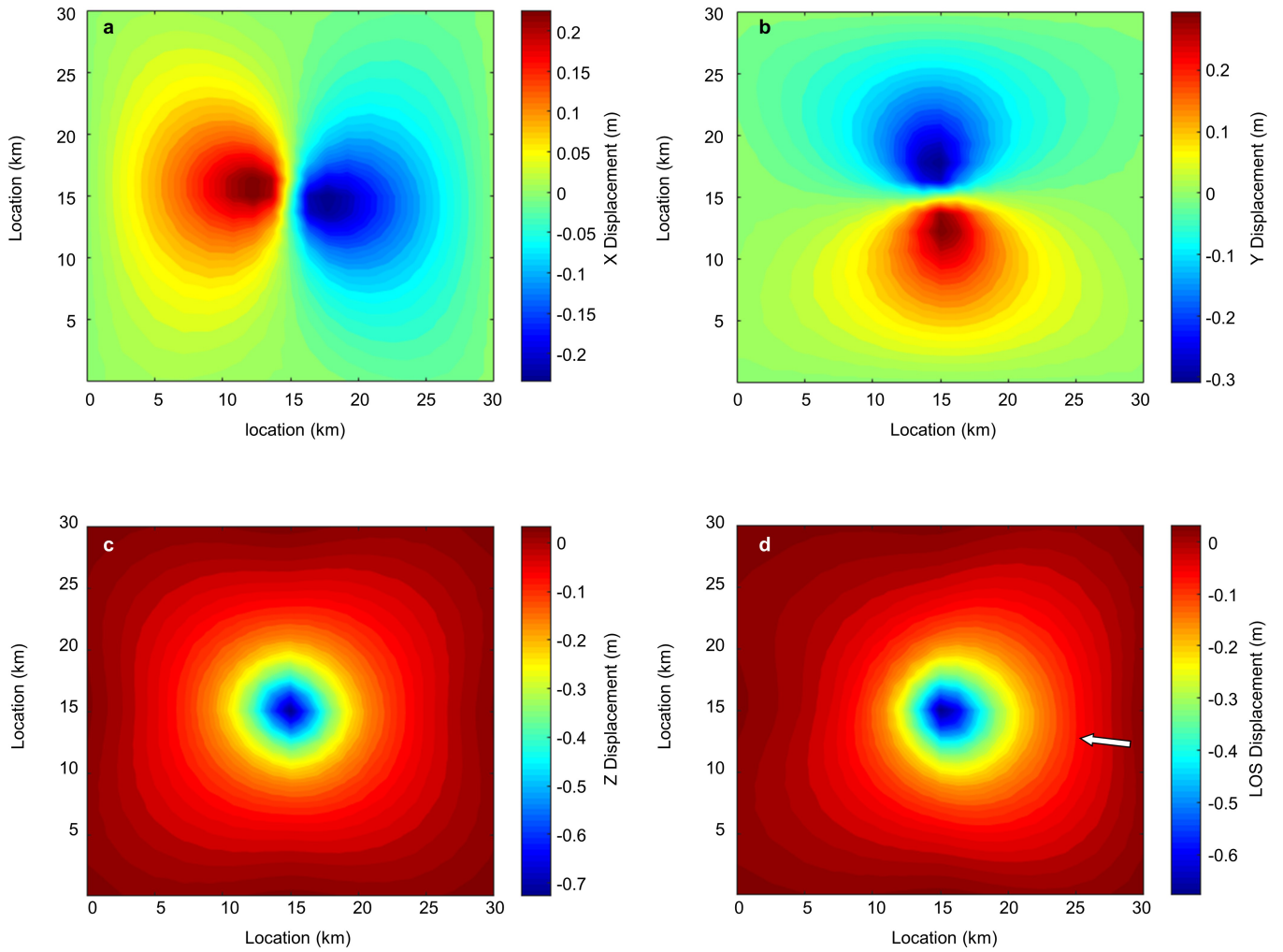
Extended Data Fig. 5 | Simulation results with lower flow rate. This simulation result is identical to that shown in Fig. 2, but with a lower flow rate, set to match the injection rate via permeability reduction. Other parameters are identical to our reference simulation (Fig. 2). **a**, Reported injection and production flow rates from the Coso field (thin lines) and simulation (bold lines). **b**, Ground deformation recovered from InSAR measurements between May 1996 and June 1998¹⁴. Image adapted with permission from ref. ¹⁴, American

Geophysical Union. **c**, Cumulative line-of-sight (LOS) surface displacement at the end of the simulation (year 30). The white arrow shows the line-of-sight unit vector $(0.38, -0.09, 0.92)^{14}$. **d**, Time evolution of maximum line-of-sight displacement (black line) and observations (blue solid lines)^{14,33,34}, along with their extrapolations (blue dashed lines). **e**, Shear stress at the end of the simulation (year 30) in the orientation parallel to the $M_w = 7.1$ rupture in the reservoir area (inset).

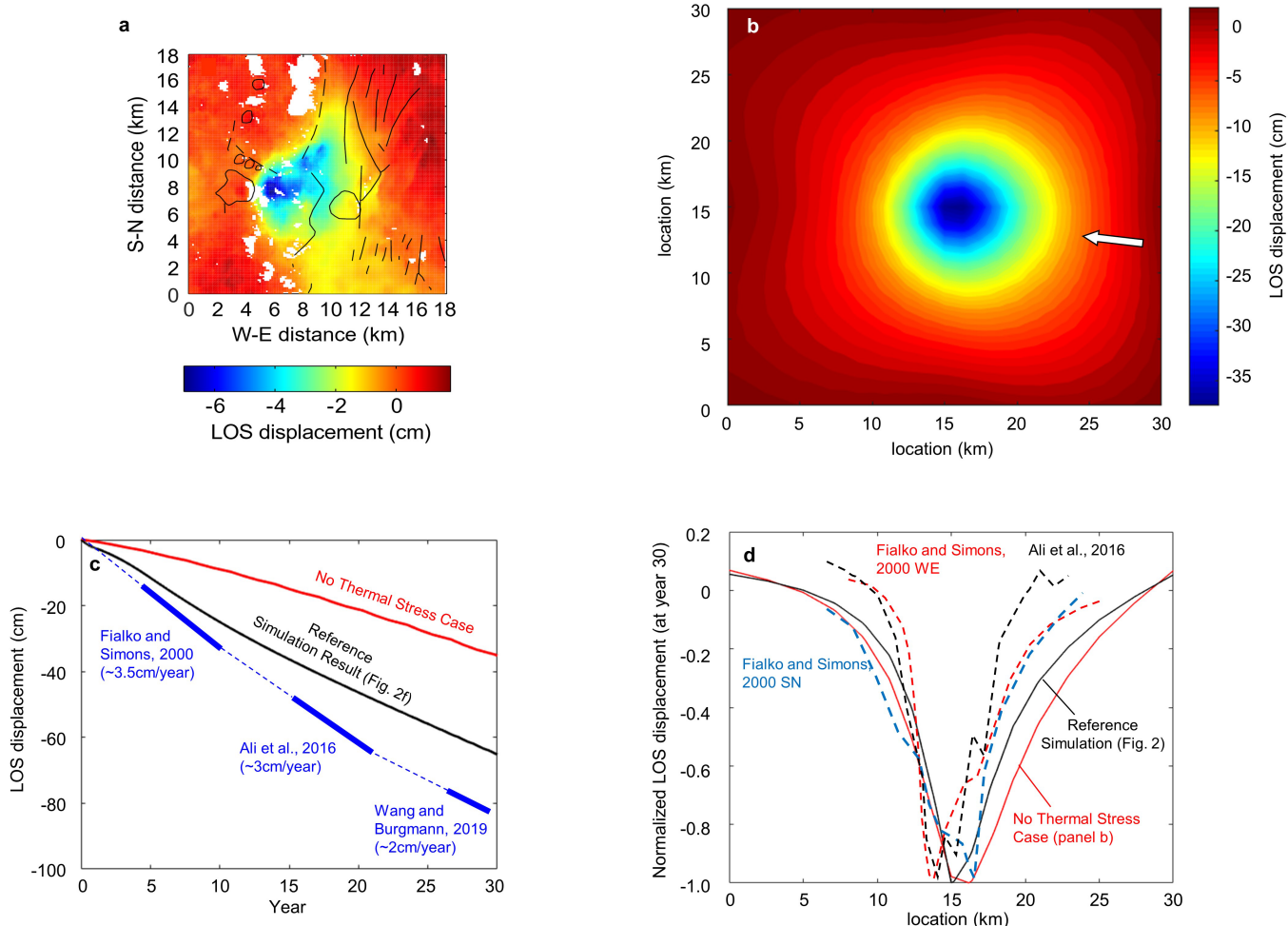


Extended Data Fig. 6 | Well bore and reservoir pressure. **a**, Pressure change at well bores (black straight line) and well blocks (the block where the imaginary well bore is embedded; coloured lines). The pressure gap between the well bore and well block is larger at injection than at production, owing to

the low temperature and consequent low fluid viscosity. **b**, Pressure drop distribution at the end of the simulation. The white rectangle indicates the $4 \text{ km} \times 4 \text{ km} \times 3 \text{ km}$ reservoir area. The pressure drops by around 5.5 MPa in the reservoir, and the halo of pressure drop extends beyond the reservoir area.

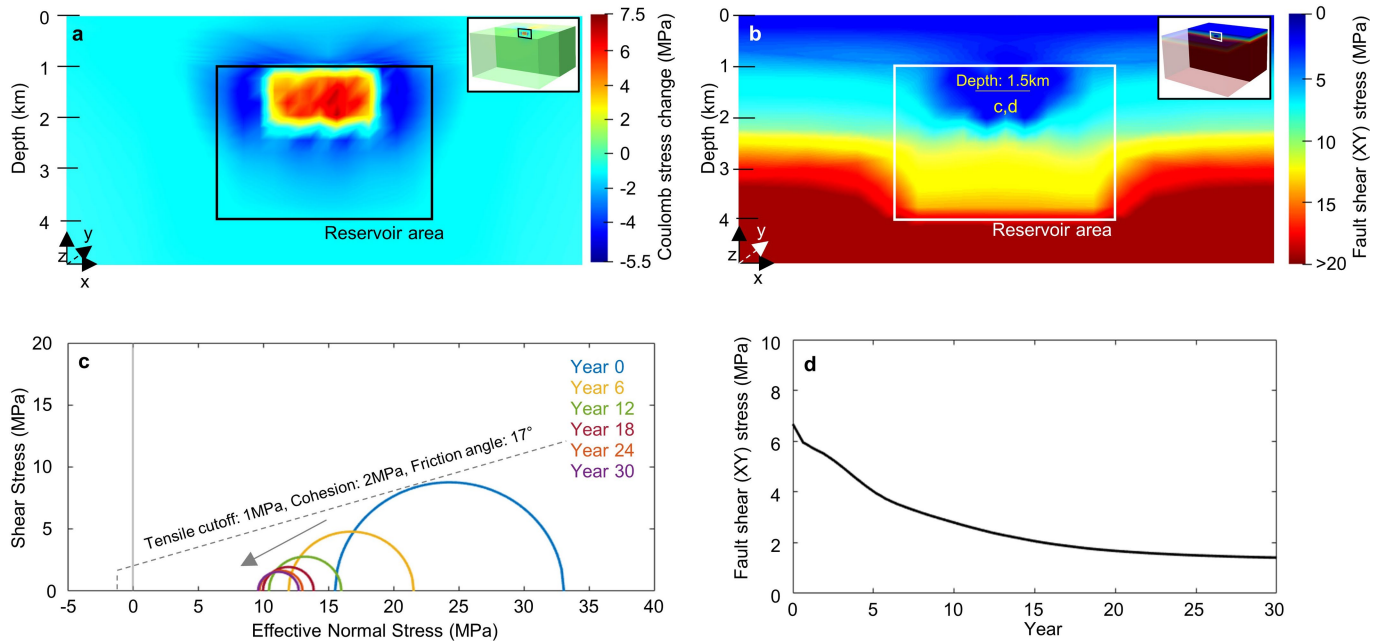


Extended Data Fig. 7 | Predicted surface displacements at the end of the reference simulation. a–d, Displacement along the x (a), y (b) and z (c) axes and line-of-sight displacement (d; identical to Fig. 2e). The white arrow denotes the azimuth of the line-of-sight vector $(0.38, -0.09, 0.92)^T$.



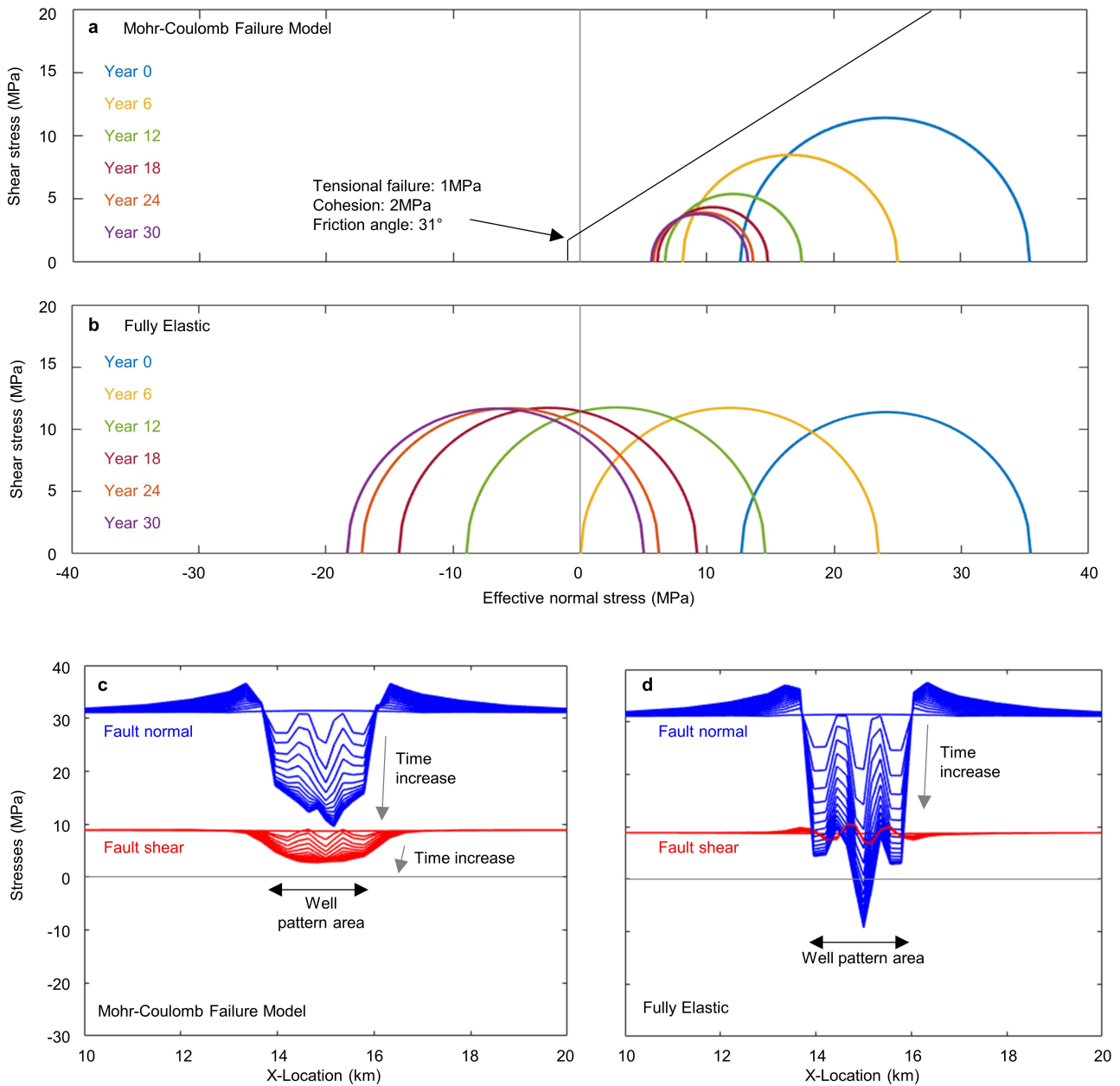
Extended Data Fig. 8 | Predicted surface deformation due to changes in pore pressure alone. **a**, Line-of-sight surface displacement recovered from InSAR measurements between May 1996 and June 1998 (identical to Fig. 2d). Image adapted with permission from ref. ¹⁴, American Geophysical Union. **b**, Predicted line-of-sight surface displacement at the end of the isothermal simulation. All parameters are identical to those for the reference simulation (Fig. 2), which accounts for thermal strain. **c**, Time evolution of maximum line-of-sight displacement of the isothermal (red) and non-isothermal (black; Fig. 2f) simulations, together with observations (blue solid lines)^{14,33,34} and their interpolations (blue dashed lines). The 'no thermal stress case' represents the

subsidence from pressure depletion alone. **d**, Observed and predicted ground displacements projected along the line of sight (arrow in **b**) of the InSAR images^{14,33}. The black solid lines are from our reference simulation (Fig. 2); the red solid line is from the isothermal simulation (no thermal strain). The curves are normalized by the maximum displacement of about 65 cm and about 35 cm for the reference and no-thermal-stress cases, respectively (**c**). The case from ref. ¹⁴ is measured between September 1993 and May 1996, with a maximum displacement of about 8 cm (west-east) and about 5 cm (south-north); the case from ref. ³³ is measured between February 2008 and October 2009, with a maximum displacement of around 2 cm.



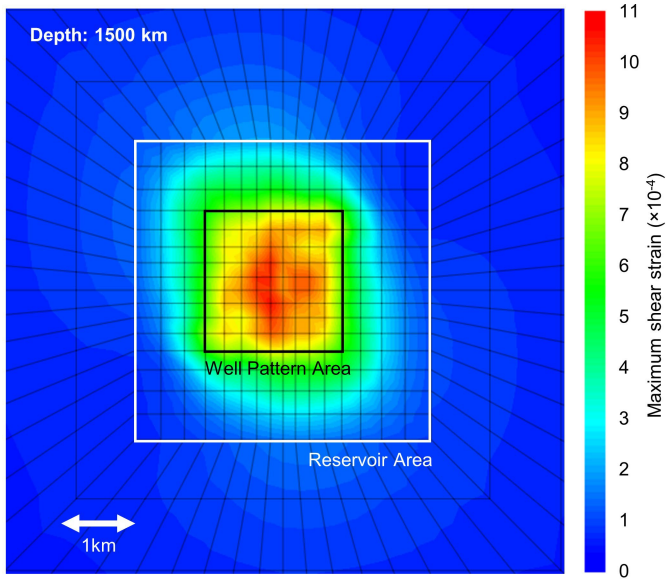
Extended Data Fig. 9 | Predicted stress changes in a simulation with reduced friction. The simulation geometry and parameters are identical to those for the reference simulation (Fig. 3), except for a lower internal friction coefficient of 0.3. **a**, Change in Coulomb stress at the end of the simulation (year 30), calculated for faults parallel to the main rupture (inset). **b**, Shear stress at the end of the simulation (year 30). Shear stress in the reservoir area (white rectangle) is strongly depleted owing to rock failure. **c**, Mohr circle

representation of stress changes during the simulation. Maximum and minimum effective normal stress are calculated at the centre of the reservoir (stresses averaged along the yellow line in **b**). The Mohr circle at year 0 is smaller than for the higher friction cases (Fig. 3c) owing to initial failure. The grey dashed line indicates the input failure criteria in this simulation. **d**, Change in shear stress at the centre of the reservoir (averaged along the yellow line in **b**).



Extended Data Fig. 10 | Comparison between fully elastic and Mohr-Coulomb failure models. a, As in Fig. 3c. **b**, As in **a**, except that the reservoir is fully elastic (no failure). When the reservoir is fully elastic (that is, when failure and the resulting drop in stress are neglected), normal stresses become impossibly large in tension. **c**, **d** Evolution of normal and shear stress relative to the orientation of the Ridgecrest fault (Extended Data Fig. 4, inset) at a depth of 1,500 m, for the Mohr-Coulomb failure model (**c**) the fully elastic model (**d**).

With the failure model (**c**), the stresses naturally approach zero over time, as a result of shear and tensile failure; in the fully elastic case (**d**), normal stresses transit through zero and become highly tensile when the shear stress drops, as a result of failure being ignored. The wiggles in the well pattern area of the reservoir are due to the non-uniform distribution of temperature driving differential thermal stresses.



Extended Data Fig. 11 | Cumulative shear strain at the conclusion of the reference simulation (after 30 years of production). The largest change in strain occurs in the well pattern area, where the change in temperature is largest. The maximum shear strain is about 1.1×10^{-3} , which is approximately two orders of magnitude larger than the strain released by seismicity, as estimated from the sum of all seismic moments (see text).

Extended Data Table 1 | Simulation model parameters

Property	Value	Property	Value
Porosity	0.2	Bulk Modulus	13 GPa
Reservoir Permeability*	1.6×10 ⁻¹⁴ m ² (~16 md) 1.0×10 ⁻¹⁴ m ² (~10 md)	Poisson's ratio	0.2
Host Rock Permeability	5 ×10 ⁻¹⁷ m ² (~0.05 md)	Vol. thermal contraction coef.	6.0x10 ⁻⁵ /K
Friction	0.6	Vol. heat capacity of rock	2156 kJ/m ³ ·K
Cohesion	2 MPa	Tensile cutoff	1 MPa
Effective density for z stress	1400 kg/m ³	Rock thermal conductivity	2.3 J/s·m·K
Initial Production over-pressure	-1 MPa	Injection Temperature	30 °C
Initial Injection over-pressure	5 MPa	Reservoir Temperature	250 °C

*1.6 ×10⁻¹⁴ m² and 1.0 ×10⁻¹⁴ m² for high and low flow rates, respectively.